JACS Au
AN OPEN ACCESS JOURNAL OF THE AMERICAN CHEMICAL SOCIETY

pubs.acs.org/jacsau
Article

Unsaturated Penta-Coordinated Mo_{5c}^{5+} Sites Enabled Low-Temperature Oxidation of C−H Bonds in Ethers

Qi Yang, Xiujuan Gao, Faen Song, Xiaoxing Wang, Tao Zhang,* Pan Xiong, Yunxing Bai, Xingchen Liu, Xiaoyan Liu, Junfeng Zhang,* Gang Fu, Yisheng Tan, Yizhuo Han, and Qingde Zhang*

Cite This: JACS Au 2023, 3, 3141−3154
Read Online

ACCESS | Metrics & More | Article Recommendations | Supporting Information

ABSTRACT: Selective oxidation of C−H bonds under mild conditions is one of the most important and challenging issues in utilization of energy-related molecules. Molybdenum oxide nanostructures containing Mo^{5+} species are effective for these reactions, but the accurate identification of the structure of active Mo^{5+} species and the catalytic mechanism remain unclear. Herein, unsaturated penta-coordinated Mo_{5c}^{5+} with a high fraction in MoO_x fabricated by the hydrothermal method were identified as the active sites for low-temperature oxidation of dimethyl ether (DME) by the deep correlation of characterizations, density functional theory calculations, and activity results, giving a methyl formate selectivity of 96.3% and DME conversion of 12.5% at unreported 110 °C. Low-temperature electron spin resonance (ESR) and *quasi in situ* X-ray photoelectron spectra (XPS) with the designed experiments confirm that the Mo_{5c}^{5+} species can be formed in situ. Molybdenum located at the pentachronic site is preferable to significantly promote the oxidation of the C−H bond in CH_3O* at lower temperatures.

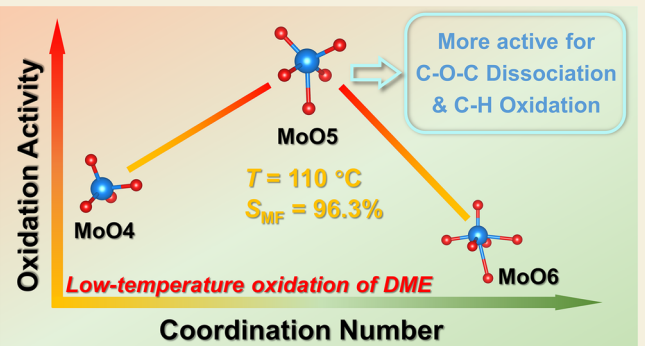

KEYWORDS: *low-temperature oxidation, activation of C−H bond, unsaturated penta-coordinated Mo_{5c}^{5+}, dimethyl ether*

INTRODUCTION

Selective oxidation catalysis is one of the most significant and challenging topics in chemistry. The selective oxidation of alkanes, alkenes, alcohols, *etc.* enables the manufacture of various high-value-added chemicals.[1−3] Despite the relative ease of C−H activation/oxidation in alcohols/ethers compared with alkanes, the oriented oxidation conversion of alcohols/ethers including C−H and C−O bonds to oxygenated compounds is a remarkable research direction, which has been paid increasing attention. However, it is not as easy to realize the targeted C−H bond breaking of alcohols/ethers under mild conditions as thought. Especially for compounds such as methanol, dimethyl ether (DME), *etc.*, if not well controlled, competitive side reactions[4] or excessive oxidation (generating CO_x) are easy to occur due to the relatively high stability of the C−H bond in these molecules, which makes the reaction difficult to achieve the oriented synthesis of key intermediate species or products.[5] In this way, designing the highly efficient catalysts, revealing the mechanism for the activation and oxidation of the C−H bond and realizing the highly selective synthesis of targeted products under mild conditions, becomes quite necessary and important but more challenging.[6,7]

Molybdenum-based catalysts are frequently utilized to activate C−H bonds to achieve oxidation or dehydrogenation of reactants at low temperatures due to the abundant coordination of oxygen and variable valence. As indicated by literature,[8,9] the state of Mo species on the catalyst surface depends on its dispersion and the surface properties of the support for the activation of C−H bonds. Handzlik and Sautet predicted with density functional theory (DFT) calculations that only in strict dehydrated conditions, Mo_2O_8 and Mo_2O_{10} dioxo species probably present on the minority (100) surface of γ-alumina are the potential precursor of the most active sites for alkene metathesis; however, a deeper revelation for catalysis mechanism was not mentioned.[10] Wang et al. disclosed that the partly reduced species (Mo^{5+}) and the terminal oxygen atoms of Mo═O bonds actually act as active sites for the conversion of benzyl alcohols despite the oxygen-coordinated MoO6 octahedrons being present on the surface.[11] Factually, the mono-oxo and dioxo structures for molybdenum oxides can be modulated by temperature, gas-phase composition, and loading,[12] and also an appropriate arrangement of the

Received: August 18, 2023
Revised: September 28, 2023
Accepted: October 6, 2023
Published: October 19, 2023

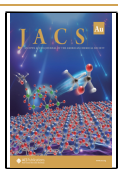

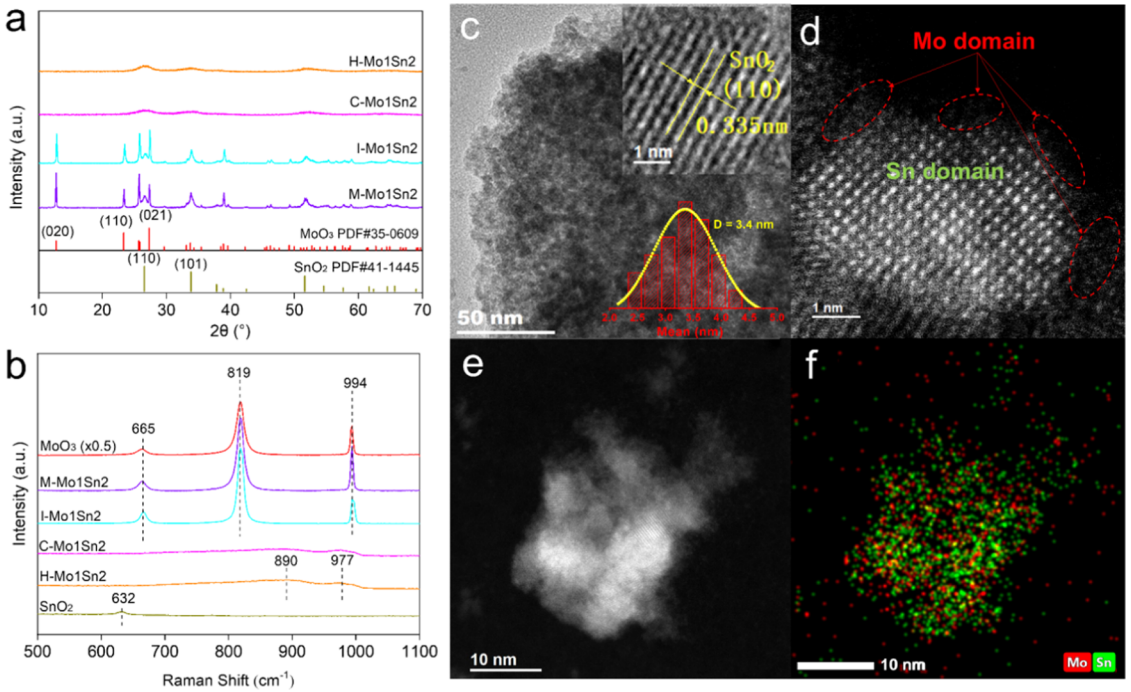

Figure 1. (a) XRD patterns and (b) Raman spectra of Mo1Sn2 catalysts prepared by different methods. (c) TEM image, (d) AC HAADF-STEM image, (e) STEM image, and (f) corresponding EDX mapping for Mo (red) and Sn (green) of the H−Mo1Sn2 catalyst.

molybdenum species interacting with the silica support significantly increases the epoxidation reactivity of propylene.[13]

Based on robust ability of Mo-based catalysts for activation and bond breaking of C−H bond, their catalytic behaviors of the selective oxidation of methanol/DME to formaldehyde, methyl formate (MF), methylal, poly(oxymethylene) dimethyl ethers, 1,2-dimethoxyethane, *etc.* at low temperatures were evaluated,[2,14−16] and the oxidation of C−H bond in CH_3O* intermediate was regarded as the rate-determining step.[9] Liu et al. discovered that the oligomeric MoO_x species loaded on SnO_2 are more capable of oxidizing DME to formaldehyde than those loaded on ZrO_2 and Al_2O_3, mainly owing to the reduced activation energy of C−H bond oxidation to HCHO over MoO_x-SnO_2.[9] The profound investigations for MoO_x-SnO_2 catalysts demonstrated that the presence of Mo−O bond of 1.94 Å benefits the formation of MF from DME oxidation (160 °C),[17] and also a minor amount of Mo^{5+} is closely related with the improved performance.[18] The above demonstrated well the enormous potential of metal oxide catalysts such as Mo in the oxidative dehydrogenation of oxygen-containing compounds. Despite so numerous efforts that have been made in the investigation of Mo-based catalysts, up to now, the precise coordination environments of Mo^{5+} atomic species in MoO_x have not been thoroughly understood. Thus, there are still vague interpretations of the confirmation of active sites and the origin of catalytic behavior in the redox cycle for low-temperature oxidation.

Herein, highly efficient H−Mo1Sn2 catalysts with abundant surface Mo^{5+} species were constructed by the hydrothermal method. The H−Mo1Sn2-O_2-500 catalyst exhibited remarkable low-temperature performance for DME oxidation, with MF selectivity up to 96.3% at 110 °C, 50 °C lower than the one reported previously. Combining the techniques of low-temperature electron spin resonance (ESR), (*quasi in situ*) X-ray photoelectron spectra (XPS), (*in situ*) X-ray absorption fine structure (XAFS), aberration-corrected high-angle annular dark-field scanning transmission electron microscopy (AC HAADF-STEM), temperature-programmed surface reaction (TPSR), *etc.*, and density functional theory calculations with catalytic performance of the catalysts, we clearly identified that the metastable Mo_{5c}^{5+} species turned out to be "real" active sites, which are able to activate the C−O bond of DME and significantly promote the oxidation of C−H bond in CH_3O* intermediate at lower temperatures. Moreover, the Mo_{5c}^{5+} active species were found to be formed *in situ* during the reaction through designing experiments. Based on $^{18}O_2$ isotope tracing experiments, a low-temperature reaction mechanism for DME oxidation to MF was proposed.

RESULTS AND DISCUSSION

Structure of Catalysts

The H−Mo1Sn2 catalyst (the molar ratio of Mo and Sn is 1:2) and the compared catalysts (C−Mo1Sn2, I−Mo1Sn2, and M-Mo1Sn2, prepared by coprecipitation, impregnation, and mechanical mixing, respectively, see the Methods in Supporting Information) were fabricated and characterized. X-ray diffraction (XRD) patterns (Figure 1a) show that the broadened characteristic diffraction peaks of tetragonal SnO_2 crystalline (PDF#41−1445) were observed on H−Mo1Sn2 and C−Mo1Sn2, whereas no characteristic diffraction peaks were assigned to MoO_3 crystalline (PDF#35−0609), indicating that molybdenum species are highly dispersed over the two catalysts. Raman shifts (Figure 1b) of 890 and 977 cm^{-1} observed on H−Mo1Sn2 and C−Mo1Sn2 are significantly different from those of the MoO_3 standard crystal (994 cm^{-1}: terminal Mo═O stretching vibration; 819 cm^{-1}: Mo−O−Mo bridged vibration) and I−Mo1Sn2 and M-Mo1Sn2. Such shifts of the former two catalysts further demonstrate the disruption of MoO_3 crystallographic structure and the formation of amorphous MoO_x species on H−Mo1Sn2 and C−Mo1Sn2 due to the stronger interaction between molybdenum oxide

https://doi.org/10.1021/jacsau.3c00479
JACS Au 2023, 3, 3141−3154

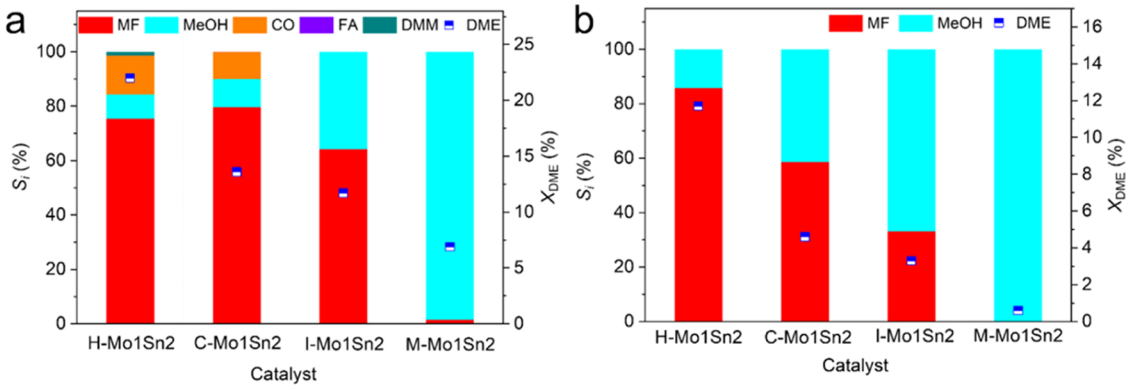

Figure 2. Evaluation data of the selective oxidation of DME over the Mo1Sn2 catalysts at (a) 150 and (b) 110 °C (reaction conditions: atmospheric pressure, $n(DME)/n(O_2)$ = 1:1, GHSV = 1800 h^{-1}).

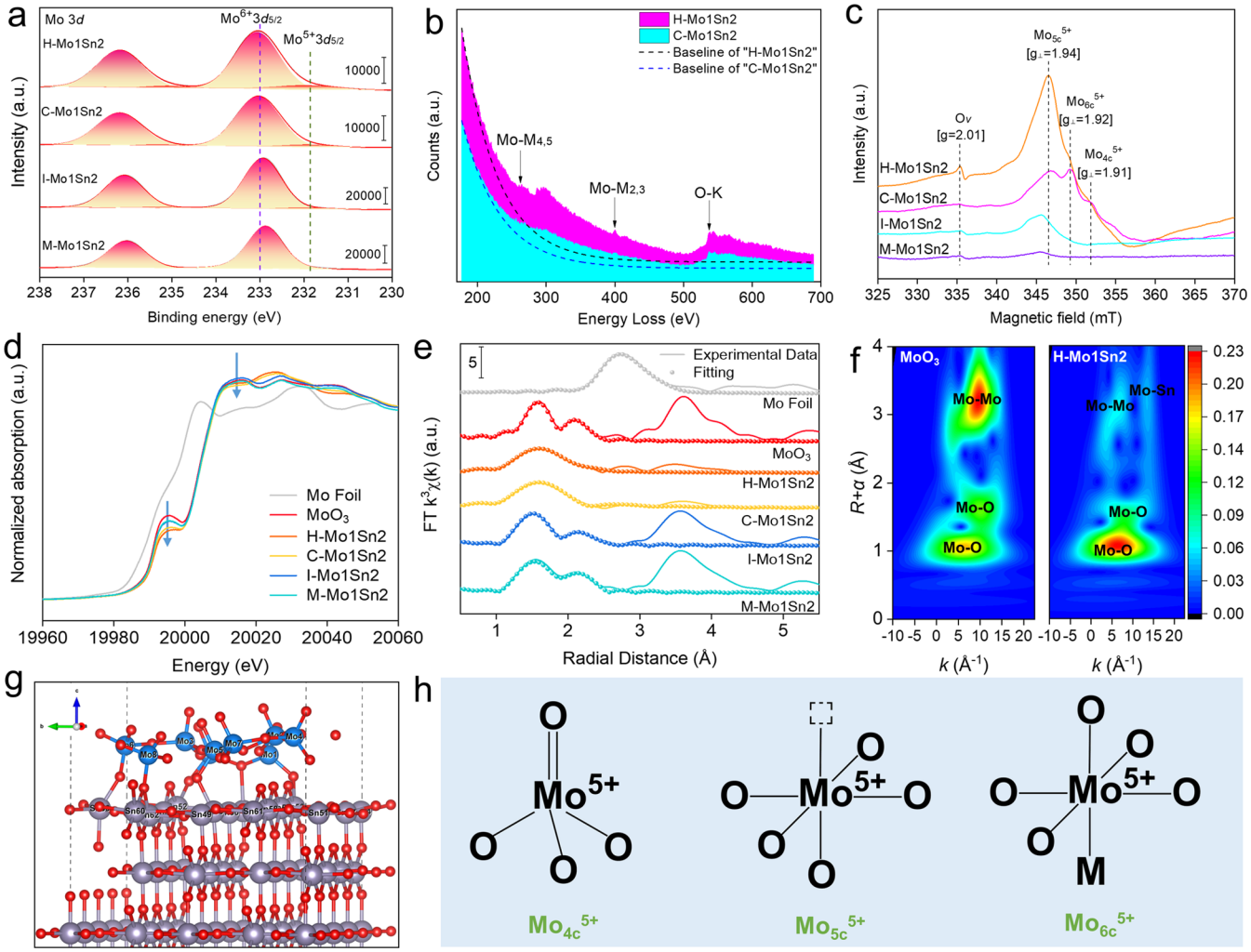

Figure 3. Characterization of the Mo1Sn2 catalysts. (a) Mo 3d XPS spectra. (b) HREELS spectra. (c) Low-temperature ESR spectra. (d) Experiment XANES spectra at the Mo K-edge. (e) k^3-Weighted (k)-function of the FT-EXAFS spectra. The solid lines represent experimental data, and the dotted lines indicate fitting results of the range from 1 to 3 Å. (f) Wavelet transform analysis of the Mo K-edge data: MoO_3 and H−Mo1Sn2. (g) Model configuration of the Mo_9O_x cluster supported on the SnO_2 (110) surface. (h) Structure of Mo^{5+} species: Mo_{4c}^{5+}, Mo_{5c}^{5+}, and Mo_{6c}^{5+}.

and tin oxide.[17,19,20] These results are further confirmed from TEM and HAADF-STEM images, where amorphous MoO_x species without well-defined crystalline shapes are homogeneously dispersed on SnO_2 with the predominance of (110) crystal plane (Figure 1c) and the disordered Mo atomic species (the scattered dark spots) are surrounded by SnO_2 nanoparticles (the orderly bright spots assigned to Sn domain, Figure 1d), also indicated by energy-dispersive X-ray spectroscopy (EDX) mapping (Figure 1e,f) results. Carefully comparing H−Mo1Sn2 and C−Mo1Sn2, the latter (Figure

https://doi.org/10.1021/jacsau.3c00479
JACS Au 2023, 3, 3141−3154

S1a) showed severe aggregation of the particles. In the case of I−Mo1Sn2 (Figure S1b) and M-Mo1Sn2 (Figure S1c), both MoO_3 and SnO_2 crystals are distinctly observed with an uneven particle size distribution. The textual properties of the prepared catalysts (Figure S2 and Table S1) also suggest that the H−Mo1Sn2 catalyst has the largest specific surface area (~118.33 $m^2 \cdot g^{-1}$) and the characteristics of a mesoporous structure (~3.45 nm) compared with others. The above observation certainly demonstrates that the hydrothermal method is quite effective in preparing a high-dispersion Mo−Sn catalyst as well as enhancing a good integrative effect.

Catalyst Performance

The activities of Mo1Sn2 catalysts were evaluated at different temperatures (Figure 2 and Table S2) for DME selective oxidation. The H−Mo1Sn2 catalyst exhibits an obviously enhanced catalytic performance at 150 °C (Figure 2a), wherein the selectivity of MF reaches 77.6% with a higher DME conversion of 22.0%. A similar MF selectivity is obtained over C−Mo1Sn2, whereas the DME conversion is only 13.6%. In addition, I−Mo1Sn2 with crystalline MoO_3 exhibits a lower catalytic activity and MF selectivity than H−Mo1Sn2 and C−Mo1Sn2 with amorphous MoO_x. Different from the above catalysts, MF is hardly formed on the M-Mo1Sn2 catalyst.

Considering that low-temperature operation assists the structural stability of Mo1Sn2 catalysts and the increase of the MF selectivity, we further tested the prepared catalysts at a lower temperature (Figure 2b). Notably, the H−Mo1Sn2 catalyst is still workable at 110 °C, obtaining the DME conversion of 11.7% and MF selectivity rising to 85.8%, without the formation of CO_x. Such a low temperature has not been reported, wherein previously high activity was obtained at 150−160 °C.[17,18,21] In contrast, other catalysts show obviously decreased activity, and the MF selectivity and DME conversion are below 60.0 and 5.0%, respectively. The better activity and MF selectivity obtained on H−Mo1Sn2 over a wide temperature range indicate that the MoO_x active structures formed on H−Mo1Sn2 facilitate the dissociation of the C−O bond in DME and the oxidation of the C−H bond in CH_3O* intermediates, especially at low temperatures. In contrast, the poor activity of I−Mo1Sn2 and M-Mo1Sn2 illustrates that it is difficult for crystalline MoO_3 to break C−O bonds at low temperatures, thus hindering the subsequent selective oxidation of C−H bonds. The difference in catalytic performance suggests that the highly active sites arise from MoO_x structures, which are remarkably more active than MoO_3.

Identification of the Low-Temperature Active Sites

Differences in the electronic nature between MoO_x-SnO_2 and MoO_3−SnO_2 catalysts were identified by XPS measurement. The results indicate that the oxidation state of Sn for all catalysts is Sn^{4+} (Figure S3a),[22] while the binding energy of Mo 3d is significantly altered. The deconvoluted peaks of Mo 3d spectra (Figure 3a and Table S3) centered at 233.0 (±0.1) and 231.9 (±0.1) eV are assigned to Mo^{6+} $3d_{5/2}$ and Mo^{5+} $3d_{5/2}$, respectively.[23,24] It suggests that Mo^{6+} and Mo^{5+} species coexist on the H−Mo1Sn2, C−Mo1Sn2, and I−Mo1Sn2 catalysts. Conversely, no signal for Mo^{5+} was detected on the M-Mo1Sn2 catalyst. The $Mo^{5+}/(Mo^{6+} + Mo^{5+})$ ratio of H−Mo1Sn2 reaches 8.4%, much higher than those of the C−Mo1Sn2 (4.5%) and I−Mo1Sn2 catalysts (4.0%). The difference in Mo^{5+} content demonstrates that Mo^{5+} species are more readily available on the oligomeric MoO_x than the crystalline MoO_3. Furthermore, the fundamental origin of the differences in the Mo element valence states of the H−Mo1Sn2 and C−Mo1Sn2 catalysts was further revealed by the high-resolution electron energy loss spectra (HREELS, Figure 3b). Ionization loss peaks for Mo-$M_{4,5}$ and Mo-$M_{2,3}$ appeared in the high energy-loss region, which is associated with the incident electron beams losing larger amounts of energy after inelastic scattering with Mo atoms.[25−27] During the inelastic scattering, the inner core electrons of Mo atoms were excited and transitioned to the $M_{4,5}$ and $M_{2,3}$ outer shells to become valence electrons. Compared with the C−Mo1Sn2 catalyst, the H−Mo1Sn2 catalyst shows relatively higher intensity of Mo-$M_{4,5}$ and Mo-$M_{2,3}$, indicating that the Mo atoms in this catalyst are prone to become active *via* internal electron excitation, promising a different valence distribution of Mo *via* electron transfer.

The essential structural diversities of Mo^{5+} species were further identified by employing a low-temperature ESR (−173 °C). Three different signals (Figure 3c) with *g* values of 1.91, 1.92, and 1.94 are assigned to tetracoordinate (Mo_{4c}^{5+}), hexacoordinate (Mo_{6c}^{5+}), and pentacoordinate (Mo_{5c}^{5+}), respectively.[28−31] Notably, the coordination environments of Mo^{5+} species in the H−Mo1Sn2 and C−Mo1Sn2 catalysts are fundamentally different, although both of them possess an oligomeric MoO_x structure. Mo^{5+} species over H−Mo1Sn2 is dominantly present in the pentacoordinate Mo_{5c}^{5+} with a much higher signal intensity than that over C−Mo1Sn2 with three homogeneously distributed coordinated Mo^{5+} species. The low intensity of the signals of Mo^{5+} species in the I−Mo1Sn2 catalyst suggests that the impregnation method is disadvantageous to generating Mo^{5+} species. The extremely weak interaction between Mo and Sn on the M-Mo1Sn2 catalyst is unable to affect the valence of the Mo species. Additionally, a strong signal at $g = 2.01$, assigned to the oxygen vacancy (O_v),[32,33] is observed over H−Mo1Sn2, which is closely related to the unsaturated Mo^{5+} species.

We then clarified the coordination environments of molybdenum species through X-ray absorption fine structure (XAFS) measurements.[34] The normalized Mo K-edge X-ray absorption near-edge structure (XANES) (Figure 3d) shows that the absorption edge for the Mo component in the Mo1Sn2 catalysts is close to that in the MoO_3 crystalline, while the intensities of the pre-edge peaks (19,990−20,000 eV) and the white-line peaks (around 20012 eV) of H−Mo1Sn2 and C−Mo1Sn2 are somewhat lower than that of MoO_3. The decrease in the intensity of pre-edge peaks is attributed to the distortion or destruction of the crystal structure while the reduction of white-line peak intensity is assigned to the partial reduction of Mo^{6+} species[35] for these two catalysts, consistent with the XPS results. Fourier-transformed extended X-ray absorption fine structure (FT-EXAFS) analysis was further performed to reveal the local environment of Mo atoms in these Mo1Sn2 catalysts (Figure 3e and Table S4). With the assistance of wavelet transform analysis (WTA) (Figures 3f and S4), the peaks at ~1.77 and 2.04 Å in the H−Mo1Sn2 catalyst are assigned to the Mo═O and Mo−O bonds,[26,36,37] wherein the fitting results of the corresponding FT-EXAFS spectra (range: 1−3 Å) show that the coordination number (CN) of O atoms in the first and second shells of Mo atoms for H−Mo1Sn2 are ~2.0 and 2.4, respectively, much lower than those of MoO_3 reference and other Mo1Sn2 catalysts. From Table S4, MoO_3 shows five Mo−O bonds originated from the linkage between the Mo atom and the O atoms

https://doi.org/10.1021/jacsau.3c00479
JACS Au 2023, 3, 3141−3154

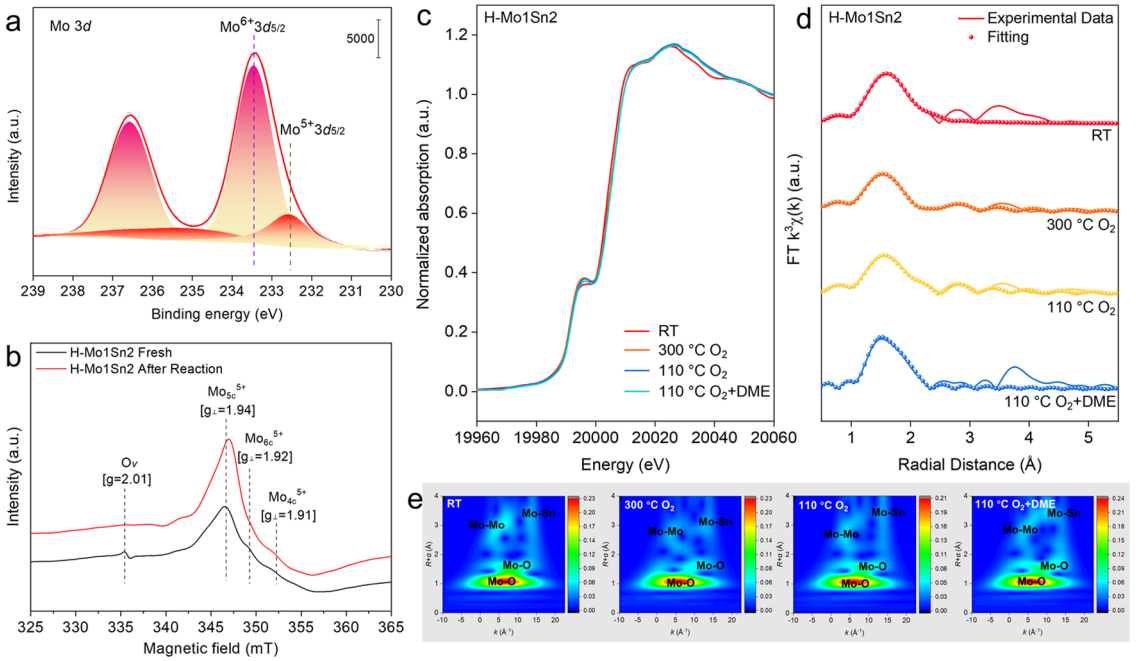

Figure 4. (a) *Quasi in situ* XPS Mo 3d spectra of the H−Mo1Sn2 catalyst recorded under reaction conditions (110 °C, n(DME)/n(O_2) = 1:1). (b) Low-temperature ESR spectra of the fresh and used H−Mo1Sn2−500 catalysts. (c) Experiment *in situ* XANES spectra at the Mo K-edge of the H−Mo1Sn2 catalyst recorded under reaction conditions (RT: room temperature; 300 °C O_2: activation at 300 °C under an O_2 atmosphere; 110 °C O_2: decrease to reaction temperature 110 °C under an O_2 atmosphere; 110 °C O_2 + DME: reaction at 110 °C with O_2 and DME). (d) k^3-weighted (k)-function of the *in situ* FT-EXAFS spectra. The solid lines are experimental data and the dotted lines are fitting results of the range from 1 to 3 Å. (e) Wavelet transform analysis of Mo K-edge data: the H−Mo1Sn2 catalyst under different procedures.

located at two layers. However, there are only two Mo−O bonds observed on H−Mo1Sn2 (~1.77 and 2.04 Å) and C−Mo1Sn2 (~1.75 and 1.92 Å), indicating that new MoO_x species formed, probably arising from the severe distortion of MoO_3 and/or absorbance of the array of Mo and O atoms similar to the MoO_3 crystallographic structure. This is indicated by no observation of the Mo−O bond of ~2.32 Å, which represents the Mo−O−Mo linkages originating from the interaction of the Mo and O atoms located at the different layers. The array of Mo−O bonds in I−Mo1Sn2 and M-Mo1Sn2 is similar to the standard MoO_3 crystal, probably owing to the maintenance of the MoO_3 phase as demonstrated by the XRD result. In conjunction with the unsaturated coordination of Mo atoms and the unique character of the Mo−O bonds identified by XAFS, the formation of Mo_{5c}^{5+} (Figure 3h) can be attributed to the distortion of the octahedral MoO6 structure and departure of one of the terminal O atoms. Additionally, the signal at a longer radial distance (3−4 Å) in the FT-EXAFS and WTA spectra for H−Mo1Sn2 shows an extra peak, which is assigned to the scattering path of Mo−O−Sn.[18,35] By adopting ab initio molecular dynamics (AIMD) simulations and DFT calculations, we further studied the influence of SnO_2 on the configurations of Mo oxides, and the result is shown in Figure S5. The calculation started from a Mo_9O_x oxide cluster loaded on the SnO_2 (110) surface. This model catalyst was constructed based on the observation of TEM where SnO_2 exposed the (110) surfaces. As expected, after adsorption, the Mo atoms interacted with the O atoms exposed on the surface of SnO_2 (110) (Figure 3g), forming Mo−O−Sn bonds (Figure S5a,b and Table S5). Owing to the interaction, the configurations of molybdenum oxide change from crystalline geometry to a highly dispersed amorphous structure on the surface of SnO_2 (110) (Figure S5c), which is in agreement with the observation of XRD and HAADF-STEM. Moreover, the results of Bader charge analysis (Figure S5d) illustrate that the charge distribution of Mo atoms in the Mo_9O_x cluster is between 2.21 and 2.30 lel, much lower than that of saturated MoO6 structure (a model structure to represent MoO_3 crystalline catalyst, Table S10) where the charge is about 2.35 lel. The decreased Bader charge of Mo confirms that electron transfer occurred between tin oxide and molybdenum oxide of the MoO_x cluster catalysts. The combination of theoretical calculations and characterization results clearly demonstrates the unique interactions between Mo and Sn species because the structures and electronic properties of the molybdenum oxide can be modulated by tin oxide.

To further investigate the evolution of Mo^{5+} species during the oxidation reaction of DME, *quasi in situ* XPS (after reacting for 1 h in an XPS cell under real conditions, the catalyst was quickly cooled and transferred to the vacuum chamber) and low-temperature ESR (measured immediately after the reaction) measurements were performed. The unchanged binding energy of Sn 3d (Figure S6) demonstrates that the oxidability of the catalysts highly depends on the metastable Mo^{n+} species. Figure 4a shows that the Mo oxidation state is a combination of Mo^{5+} and Mo^{6+}, with no signals for Mo^{4+} or other lower valence states. The quantified results (Table S6) show that the proportion of Mo^{5+} in the H−Mo1Sn2 increases from 8.4% (fresh) to 19.0% after the reaction. The variation of the content of Mo^{5+} and Mo^{6+} species explains that the redox cycle may take place between Mo^{6+} and Mo^{5+} at 110 °C. Noteworthy, the increased Mo^{5+} is evidenced to be primarily Mo_{5c}^{5+}, based on the substantially enhanced intensity of the Mo_{5c}^{5+} peak in the ESR signals of the fresh and used H−

https://doi.org/10.1021/jacsau.3c00479
JACS Au 2023, 3, 3141−3154

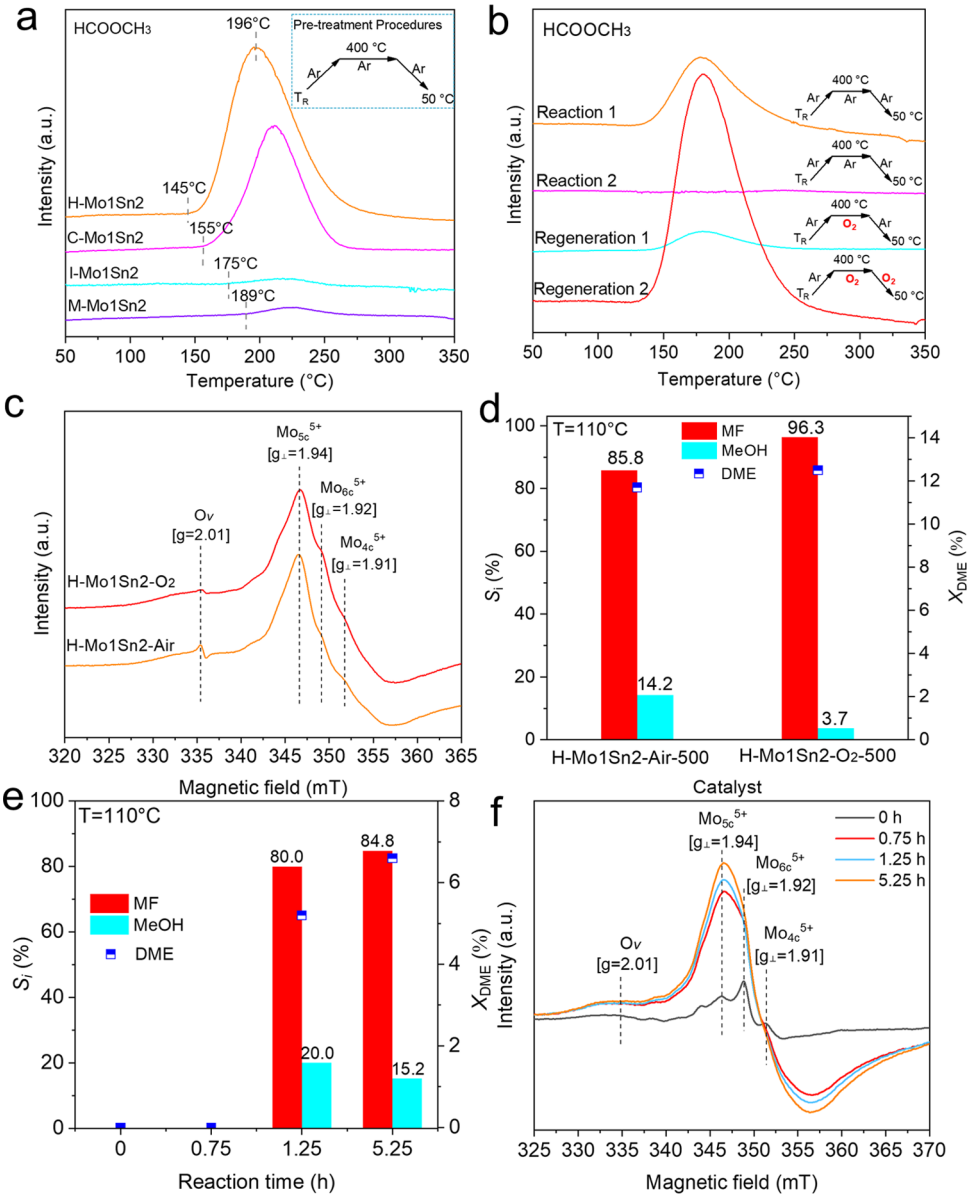

Figure 5. (a) DME-TPSR-MS spectra of the Mo1Sn2 catalysts prepared by different methods, recorded under a DME flow (test conditions: DME, 30 mL·min^{-1}, 50−400 °C). (b) DME-TPSR-MS spectra of the H−Mo1Sn2 catalyst with different pretreatments by switching Ar and O_2 (detailed pretreatment procedures are shown in the section of Experimental Methods in SI). (c) Low-temperature ESR spectra and (d) evaluation data of H−Mo1Sn2-Air-500 and H−Mo1Sn2-O_2-500. (e) Evaluation data and (f) low-temperature ESR spectra of the H−Mo1Sn2-O_2-300 catalyst at different reaction times.

Mo1Sn2−500 catalysts (Figure 4b). Therefore, it suggests that the Mo_{5c}^{5+} species play a crucial role in the redox cycles.

In situ XAFS was used to explore the dynamic evolution of the coordination environment of Mo active sites by recording instantaneously during the activation and reaction stages under the corresponding atmospheres. The slight movement toward high energy of the absorption edge of the Mo K-edge (Figure 4c) is observed after heating with O_2 and/or O_2 + DME, originating from the electron transfer from Mo to O atoms, inducing the activation of the O_2 molecules. During the reaction, nevertheless, the slight migration of the absorption edge indicates that the change of the average oxidation state of Mo is not apparent. The wavelet transform analysis (Figure 4e) and FT-EXAFS (Figure 4d and Table S7) fitting results reveal the variations of the local environment of Mo atoms (joint contribution of Mo^{5+} and Mo^{6+}) at each stage. During the activation process (300 °C O_2), the distances of Mo−O bonds in the H−Mo1Sn2 catalyst are mainly ∼1.67, 1.72, and 1.95 Å, and the coordination numbers of the O atoms are ∼1.5, 1.6, and 2.5, respectively. Compared with the fitting results of static H−Mo1Sn2 (measured at room temperature without O_2), the shortening of Mo−O bonds and the increased coordination number (the total CN is about 5.6) can be assigned to enhanced Mo−O interaction resulting from the electron transfer from Mo to O and the activated oxygen atom of the O_2 molecule coordinated to the Mo center. As the temperature decreased to 110 °C, a Mo−O bond of ∼2.29 Å (CN: ∼ 1.2) appeared, which might be ascribed to the coordinated active oxygen atom transformed from the activated O_2, indicating the strong ability of unsaturated Mo species to activate and dissociate O_2 at such a low temperature. After introducing O_2 and DME at 110 °C, the radial distances of Mo−O bonds vary

https://doi.org/10.1021/jacsau.3c00479
JACS Au 2023, 3, 3141−3154

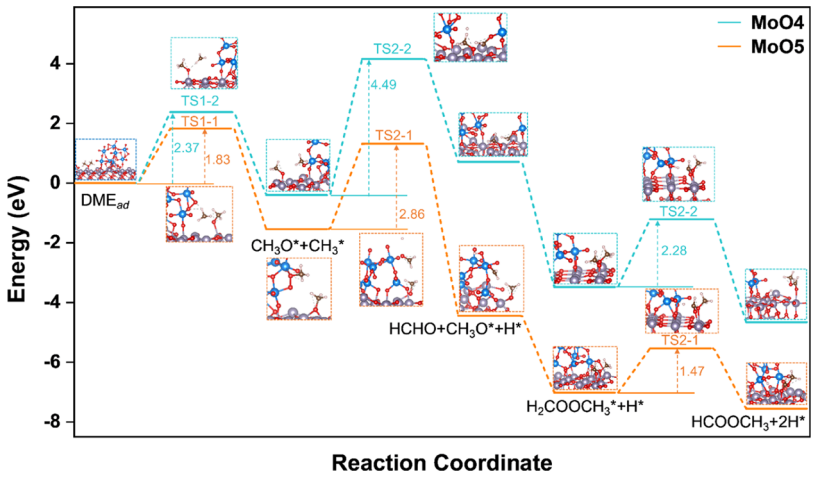

Figure 6. Potential energy surface of DME dissociation and MF formation on the $MoO_x/SnO_2(110)$ model catalyst, where *x* denotes 4 or 5 to represent the Mo atoms located at the tetra-coordinated and penta-coordinated sites.

toward relatively lower distances as the coordination number of oxygen atoms changes in a narrow range (the total CN is about 4.9). Such variations demonstrate the successful absorption/activation of DME molecules on Mo active sites. Besides, the changes in the intensity of Mo−Sn in the wavelet transform spectra (Figure 4e) illustrate the participation of the Mo−O−Sn structure, which is important to the formation of MF. Since Mo_{5c}^{5+} species are considered to be majorly contributing to the low-temperature oxidation of DME, the investigation of the coordinated oxygen bonded to Mo_{5c}^{5+} should be of great concern. Herein, DME temperature-programmed surface reaction mass spectrometry experiments were conducted (Figures 5a and S7). For H−Mo1Sn2, the lower initial formation temperature (T_i = 145 °C) and higher intensity of MF suggest that the abundant active Mo_{5c}^{5+} species are more responsive to low-temperature oxidation than other catalysts. Herein, the reasons for a higher T_i than reaction temperature (110 °C) include less catalyst dose, absence of O_2, rapid heating rate, and lagging of the mass spectrometry scanning signal. The Mars-van Krevelen mechanism[37] illustrates that the participation of active lattice oxygen, which was derived from MoO_x active structures, is predominant in the oxidation reaction under oxygen-free conditions. Following the depletion of active lattice oxygen indicated by the absence of MF generation, regeneration experiments of active sites (Figure 5b) were carried out. The results indicate that the MoO_x active species can be regenerated by the supplementation of active lattice oxygen after oxygen supplementation in the high-temperature treatment step (Regeneration 1). MF is reproduced and enhanced after the subsequent treatment with O_2 (Regeneration 2). This strongly demonstrates the reproducibility of active MoO_x species and the facilitation of chemisorbed oxygen, which is formed and stored on the oxygen vacancies of Mo_{5c}^{5+}, in line with the decreased ESR signal of O_v in Figure 3c. The DME-TPSR-MS demonstrates the high stability and powerful regeneration ability of the Mo_{5c}^{5+} active sites of H−Mo1Sn2. It meanwhile suggests that the introduction of O_2 is beneficial to improve the low-temperature oxidation performance.

Based on the findings of the important effect of oxygen, we prepared an H−Mo1Sn2-O_2-500 catalyst calcined under O_2. The low-temperature ESR spectra (Figure 5c) show that the Mo^{5+} species in H−Mo1Sn2-O_2-500 are mainly in the form of metastable pentacoordinate Mo_{5c}^{5+}. Notably, compared with H−Mo1Sn2-Air-500 (H−Mo1Sn2), a dramatic performance enhancement of the H−Mo1Sn2-O_2-500 catalyst was achieved for low-temperature oxidation of DME with the MF selectivity of 96.3% at 110 °C (Figure 5d and Table S8). Such results further support that the unsaturated-coordinate Mo_{5c}^{5+} species are the main active sites for the low-temperature oxidation of DME and the treatment with O_2 indeed increases the low-temperature performance of H−Mo1Sn2, which is entirely consistent with the results of the DME-TPSR-MS experiments.

We then designed experiments and prepared another catalyst calcined with O_2 at 300 °C (denoted as H−Mo1Sn2-O_2-300) to investigate the evolution of active Mo_{5c}^{5+} species in the reaction. Evaluation results (Figure 5e and Table S9) show that H−Mo1Sn2-O_2-300 has no activity in the initial stage (0.75 h). However, as time on stream increases to 1.25 h, the catalytic performance was presented with the DME conversion of 5.2% and MF selectivity of 80.0%. A modest increase in the catalyst activity and product selectivity was observed after reacting for 5.25 h. Low-temperature ESR spectra (Figure 5f) show that three types of coordinated Mo^{5+} species are observed on the fresh H−Mo1Sn2-O_2-300 catalyst, whereas the primary one is Mo_{6c}^{5+}, different from those of the fresh H−Mo1Sn2-O_2-500 and H−Mo1Sn2-Air-500 catalysts. As the reaction progresses, the coordination structure of Mo^{5+} significantly changes. With the increase of the exposure time of the catalyst in the reaction atmosphere, more Mo_{5c}^{5+} species are formed. Moreover, correlating the catalyst activity with the ESR signal of Mo_{5c}^{5+}, it was found that the content of Mo_{5c}^{5+} and the catalyst activity increased simultaneously with the advancing reaction duration. Such synchronous variation demonstrates that Mo_{5c}^{5+} species are really active sites and can be *in situ* formed during the low-temperature oxidation of DME.

DFT Calculation of Reaction Path of DME Oxidation to MF on the MoO5 and MoO4 Model Catalyst Surfaces

DFT calculations were performed to gain more insight into the origin of the enhanced activities of the MoO_x-SnO_2 catalyst. A model catalyst $MoO_x/SnO_2(110)$ was constructed (Figure S10),[38,39] wherein Mo atoms located at the different coordination environment and Sn atoms located on the surface of $SnO_2(110)$ were presented after a full structure optimization. The adsorption of DME and the formation of

https://doi.org/10.1021/jacsau.3c00479
JACS Au 2023, 3, 3141−3154

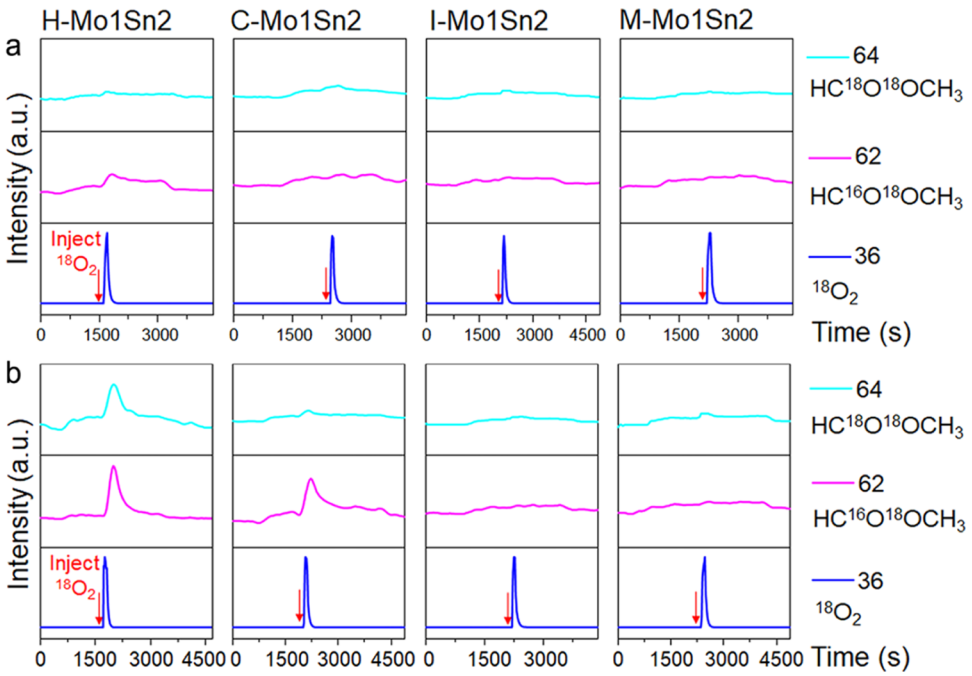

Figure 7. Mass spectra of $^{18}O_2$–IR-MS characterization of the Mo1Sn2 catalysts recorded at (a) 140 °C and (b) 200 °C (test conditions: 10% DME/Ar, 20 mL·min^{-1}, $^{18}O_2$ 20 mL, and 140 and 200 °C).

HCHO and MF were fully investigated on the optimized $MoO_x/SnO_2(110)$ system. At the beginning of the investigation, the adsorption of DME was fully studied on the surface of both the MoO_x cluster and the SnO_2 surface. As shown in Figure 6, the adsorption of DME is preferable on the Sn atom than on the MoO_x cluster, owing to the deformation of the MoO_x polyhedron. Thereafter, DME dissociated into CH_3O* and CH_3* between the Sn and Mo clusters. The MoO5 cluster is preferable to this reaction compared with the MoO4 cluster owing to the lower reaction barrier and reaction energy (1.83 and −0.30 eV for MoO5 *vs* 2.75 and 0.52 eV for MoO4). After that, CH_3* bonds with O atoms located at the terminal of the MoO_x cluster to form a new CH_3O* group. The formation of HCHO through CH_3O* on both MoO5 and MoO4 clusters is investigated subsequently. The results showed that the formation of HCHO on the MoO5 cluster is more energy preferable than on the MoO4 cluster (the reaction barriers on the two structures are 2.86 eV for MoO5 and 4.49 eV for MoO4). Through investigation on the coupling between HCHO and CH_3O*, it is noted that H_2COOCH_3* is fairly easy to form on the surface of Sn located on the $SnO_2(110)$ support, whereas the combination between HCHO and CH_3O* is not to occur owing to the long distance between the two Mo atoms located on the MoO_x cluster. The above results indicate that a coordination-unsaturated surface Sn atom is the active site for the formation of H_2COOCH_3*. Our calculated results are in accordance with the other researchers, who found that the formation of MF is very easy on SnO_2. The final step for MF formation is started from H_2COOCH_3*, which takes place on the interface between the $SnO_2(110)$ and MoO_x clusters, where the H atom was attracted by the nearby O located on the MoO_x cluster. From Figure 6, the calculated reaction barriers for MF formation are 1.47 eV for MoO5 and 2.28 eV for MoO4, respectively. Compared with the elementary reaction of DME dissociation and CH_3O* + HCHO condensation, the higher activation energy of CH_3O* oxidation (both on MoO5 and on MoO4) indicated that the oxidation of CH_3O* to HCHO* is the rate-determining step of DME oxidation to MF, in line with established understanding.[9] Based on the results of DFT calculations, the lower activation energy for the C−O bond activation in DME and the lower reaction energy for C−H bond oxidation in CH_3O* on the MoO5 cluster sufficiently illustrate that penta-coordinated MoO5 species are "real" active sites for low-temperature oxidation of DME.

Additionally, AIMD simulation was performed to study the structure evaluation of MoO_x in the presence of an O_2 atmosphere starting from the most stable configurations of molybdenum oxides located on the $SnO_2(110)$ surface. The simulation starts from a presorption configuration of the O_2 molecule located at the center of a ring surrounded by four tetra-coordinated molybdenum oxides, which was obtained from a geometry optimization. After structure optimization, an enlarged distance between O and O in the presented O_2 molecule increased from 1.128 to 1.493 Å (Figure S11b,c), indicating that O_2 was activated by the tetra-coordinated molybdenum oxide clusters. Owing to the activation of O_2, the tetra-coordinated molybdenum oxide clusters were oxidized to the penta-coordinated structure. During AIMD simulation, as the system evolves at the reaction temperature, the distance between O atoms in the presented O_2 increased gradually and the penta-coordinated Mo oxide clusters kept their structure during 2.5 ps simulation (Figure S11d,e) (from 1.128 Å in O_2 to 1.541 Å on the cluster), indicating the participation of O_2 in the formation of penta-coordinated molybdenum oxide species. During 5.0 ps AIMD simulation (Figure S11f,g), the distance between these two O atoms falls in the range of 1.493 to 1.557 Å, *i.e.*, from 1.493 Å at 1.0 ps, 1.541 Å at 2.5 ps to 1.557 Å at 5.0 ps, respectively. The O_2 adsorption and AIMD simulation results indicate that the O_2 molecule is activated during the reaction, which facilitates the activation of DME and the formation of HCHO. Furthermore, owing to the

https://doi.org/10.1021/jacsau.3c00479
JACS Au 2023, 3, 3141−3154

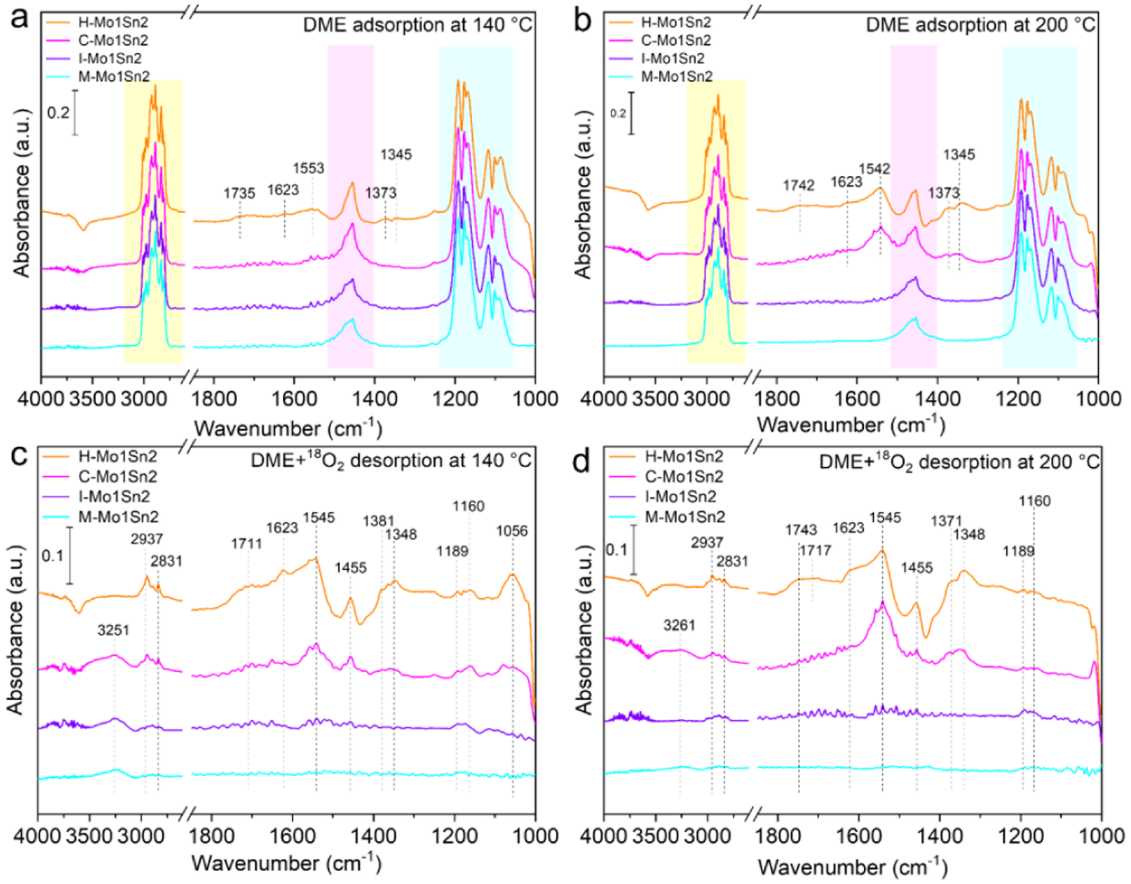

Figure 8. *In situ* DRIFT spectra of $^{18}O_2$−IR-MS characterization of the Mo1Sn2 catalysts. (a, b) The final spectra of DME adsorption at 140 and 200 °C. (c, d) The final spectra of DME + $^{18}O_2$ desorption at 140 and 200 °C.

activation of O_2, the distance between O (in O_2) and Mo changes from 2.1 to 2.3 Å, which falls in the range of Mo−O bond as shown in MoO_3 accompanied by the configuration change of tetra-coordinated molybdenum oxides to penta-coordinated molybdenum oxides. Such calculation results are in line with the observation of *in situ* XAFS, wherein the variation of Mo−O bond corresponds to the transformation of Mo−O bonds from 2.04 Å of H−Mo1Sn2-RT (initial state) to 2.29 Å of H−Mo1Sn2−110 °C + O_2. Moreover, the trend of configuration change of MoO_x after absorbing oxygen is consistent with TPSR, further confirming that the chemically adsorbed oxygen can transform into active lattice oxygen for the regeneration of low-temperature oxidation sites.

Reaction Mechanism of Low-Temperature Oxidation of DME

Despite the fact that the mechanism of high-temperature selective oxidation of DME to MF has been studied, it is still controversial,[40−42] and especially the low-temperature mechanism is even less clear. Herein, we designed $^{18}O_2$ isotope tracing tests ($^{18}O_2$−IR-MS) to reveal the low-temperature reaction mechanism by monitoring the migration of oxygen species in the DME oxidation reaction (Figure 7). $HC^{16}O^{18}OCH_3$ (m/z = 62) and $HC^{18}O^{18}OCH_3$ (m/z = 64) are detected, respectively. In those curves, extremely weak peaks are considered to signal fluctuations caused by the pulsing $^{18}O_2$. The mass spectra (Figure S12) of the H−Mo1Sn2 catalyst under different temperatures (from 110 to 200 °C) show that the first appearances of the signals at m/z = 62 and m/z = 64 are at 140 and 200 °C, respectively. Such temperatures are very close to the initial temperature of MF formation (145 °C) and the temperature of the highest yield (196 °C) in the DME-TPSR-MS. Comparing the curves recorded at 140 °C (Figure 7a), $HC^{16}O^{18}OCH_3$ is detected only on the H−Mo1Sn2 catalyst. However, when tested at 200 °C (Figure 7b), the signal for $HC^{16}O^{18}OCH_3$ is enhanced for the H−Mo1Sn2 catalyst and becomes observable for the C−Mo1Sn2 catalyst, albeit at a lower intensity. Notably, $HC^{18}O^{18}OCH_3$ only formed on the H−Mo1Sn2 catalyst at 200 °C. The present $^{18}O_2$−IR-MS experiments clearly demonstrate that the differences in $HC^{16}O^{18}OCH_3$ production over the different catalysts are related to variations in the active species, wherein the H−Mo1Sn2 catalyst featured with metastable Mo_{5c}^{5+} is more appropriate for the low-temperature reaction. The discrepancies between $HC^{16}O^{18}OCH_3$ and $HC^{18}O^{18}OCH_3$ on H−Mo1Sn2 suggest that two different reaction pathways may exist at high temperatures.

The corresponding *in situ* DRIFT spectra of DME adsorption (Figure 8a,b) showed significant variations among these Mo1Sn2 catalysts. Besides the vibrational peaks, they are attributed to $DME_{gas/ads}$. (2800−3000 cm^{-1}: C−H stretching vibrations in CH_3* and CH_2*; 1400−1500 cm^{-1}: C−H bending vibrations in CH_3* and CH_2*; 1000−1200 cm^{-1}: C−O, C−O−C stretching vibrations), and several infrared vibration peaks at 1300−1750 cm^{-1} appeared only on H−Mo1Sn2 and C−Mo1Sn2, especially on the former; the peaks are still visible at 140 °C, demonstrating its robust low-temperature activation capabilities. The observation of a special peak at 1735 cm^{-1} on H−Mo1Sn2 (Figure 8a),

https://doi.org/10.1021/jacsau.3c00479
JACS Au 2023, 3, 3141−3154

Scheme 1. Low-Temperature Oxidation Route of DME to MF over MoO5/SnO_2

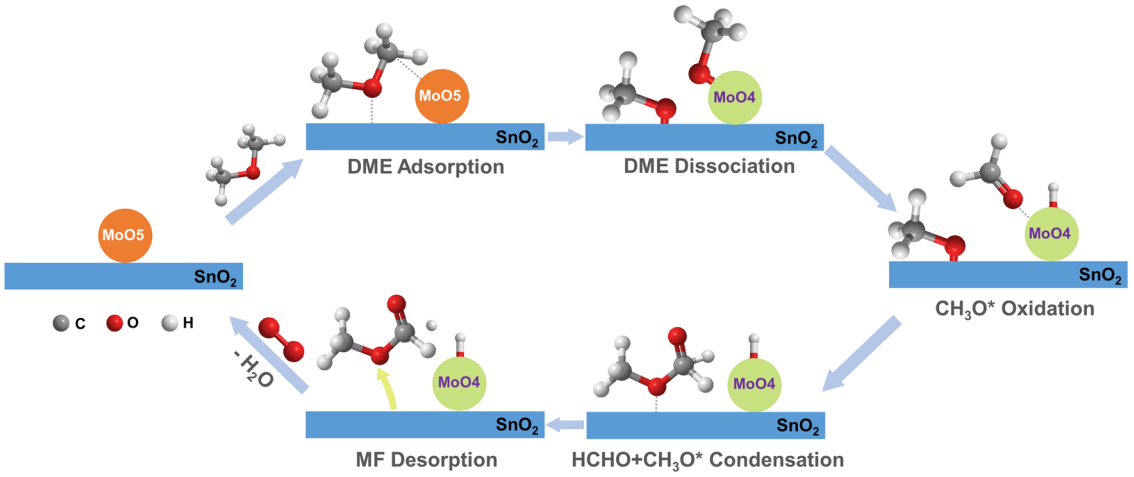

which is assigned to the C═O stretching vibration of the adsorbed HCHO,[43,44] signifies that oxidative dehydrogenation of CH_3O* species (from DME dissociation) has taken place. This phenomenon not only demonstrates that the Mo_{5c}^{5+} active sites on H−Mo1Sn2 possess the advanced low-temperature oxidation ability but also implies that the breaking of the C−H bond in CH_3O* species into HCHO is quite a pivotal step for the MF formation. From Figure 8c,d, it is observed that a series of peaks emerged and were accompanied by obvious discrepancies after the desorption of DME at 140 and 200 °C. Herein, the broad peaks at 3251−3261 cm^{-1} are assigned to the vibration of hydroxyl groups, which might have originated from the adsorbed CH_3OH; the peaks at 2937 and 2831 cm^{-1} are attributed to the C−H stretching vibrations in CH_3O*; the broad peak at around 1711−1717 cm^{-1} is ascribed to the C═O stretching vibration of the adsorbed $HCOOCH_3$;[45] the sharp peak at 1623 cm^{-1} is assigned to the vibration of hydroxyl groups in the adsorbed H_2O molecules;[45] the peaks at 1545, 1371−1381, and 1348 cm^{-1} are assigned to the monodentate formate species;[46] the peaks at 1160−1189 and 1056 cm^{-1} are attributed to the linear and bridged adsorbed methoxy groups, which adsorb on Mo and/or Sn atoms.[44,46,47] Comparing the adsorption and desorption of DME on H−Mo1Sn2 at 140 °C (Figure 8a,c), the disappearance of C═O vibration of HCHO and the appearance of C═O vibration of $HCOOCH_3$ indicate that the formation of MF is closely related with HCHO. In contrast to C−Mo1Sn2 (Figure 8c), the smaller peaks of linear adsorbed CH_3O* on H−Mo1Sn2 suggest that CH_3O* species have been consumed during MF formation. Combined with the MS signal of $HC^{16}O^{18}OCH_3$ (140 °C) in Figure 7a, we propose that the low-temperature oxidation of DME to MF depends on the intermediate reaction of $HCH^{18}O$ (from the oxidation of CH_3* bonded with MoO_x containing the ^{18}O atom) and $^{16}OCH_3$* (Sn−$^{16}OCH_3$* formed from the dissociation of DME). Such a reaction route is similar to the aldol condensation mechanism of the selective oxidation of CH_3OH, which has been revealed on Au and Cu nanoparticles.[48,49] In the case of DME desorption on H−Mo1Sn2 at 200 °C (Figure 8d), the coexistence of C═O vibrations of HCHO (1743 cm^{-1}) and $HCOOCH_3$ (1717 cm^{-1}) indicates the enhanced oxidation of CH_3O*, which can be derived from both Mo−$^{18}OCH_3$* and Sn−$^{16}OCH_3$* intermediates,[50] according to the reduction of linear adsorbed methoxy groups and the vanishing of bridged adsorbed methoxy groups. For the $HC^{16}O^{18}OCH_3$ and $HC^{18}O^{18}OCH_3$ observed on MS spectra at high temperatures, the formation of the former follows the aldol condensation mechanism, while the formation of the latter might rely on the Tishchenko reaction of $HCH^{18}O$ (dimerization).[51] Such varied phenomena apparently demonstrate that the selective oxidation of DME to MF adheres to different catalytic mechanisms at low and high temperatures, respectively. The key to the superior performance of H−Mo1Sn2 at low temperatures is the targeted selective oxidation of the C−H bond of CH_3O* to formaldehyde by the unsaturated penta-coordinated Mo_{5c}^{5+} active sites.

In combination with the above DFT calculations and $^{18}O_2$ isotope experiments, we, here, proposed a possible reaction mechanism for the low-temperature oxidation of DME to MF on a pentacoordinate MoO5 active site (as shown in Scheme 1). During the reaction, DME preferentially adsorbs on an unsaturated Sn site nearing the MoO_x species. With the assistance of the MoO5 structure, the C−O bond in DME is easily activated and broken into CH_3O* and CH_3* groups, forming Sn-OCH_3 and MoO4-OCH_3 (MoO5-CH_3). Then, the C−H bond of MoO4-OCH_3 is oxidized *via* α-H elimination to form the key intermediate HCHO, which is the rate-determining step of this reaction. Subsequently, the HCHO migrates to the SnO_2 surface and is coupled with Sn-OCH_3 to form the H_2COOCH_3* intermediate *via* hemiacetal reaction,[53,54] which finally transforms to the target product $HCOOCH_3$ after the dehydrogenation. After that, the MoO5 active structure is reformed by the remediation of reactive oxygen species, derived from O_2.

CONCLUSIONS

The key role and the coordination environment of Mo^{5+} species were comprehensively revealed at the atomic level. We confirmed that unsaturated penta-coordinated Mo_{5c}^{5+} species in the H−Mo1Sn2 catalyst prepared through the hydrothermal method were the main active sites responsible for DME highly selective oxidation to MF at 110 °C. The combination of various characterizations (low-temperature ESR, (*quasi in situ*) XPS, (*in situ*) XAFS, AC HAADF, *etc.*), theoretical calculations, and activity results demonstrated that the presence of metastable square-pyramidal Mo_{5c}^{5+} species is the essential reason for the low-temperature oxidation, which substantially reduces the reaction energy of DME dissociation

https://doi.org/10.1021/jacsau.3c00479
JACS Au 2023, 3, 3141−3154

and is more favorable for the oxidation of the C−H bond in CH_3O* to HCHO. Besides, *in situ* formed Mo_{5c}^{5+} active species are found through the designed experiments. From the $^{18}O_2$ isotopic experiments, a low-temperature mechanism of the hemiacetal reaction of CH_3O* and HCHO for DME oxidation to MF over the MoO5 active sites was proposed.

This work broadens and deepens our understanding of the coordination environments of Mo^{5+} species in MoO_x-based catalysts and their crucial role in the oxidation reaction under mild conditions. This provides a new strategy for the design of highly efficient catalysts for low-temperature oxidation of energy-related molecules in the future.

EXPERIMENTAL SECTION

Materials

$(NH_4)_6MoO_7O_{24}\cdot 4H_2O$ (>99%) was purchased from Tianjin Guangfu Technology Development Co., Ltd. $SnCl_4\cdot 5H_2O$ (>99%) was purchased from Aladdin Industrial Corporation. All chemicals were purchased and used without further purification.

Catalyst Preparation Methodology

The representative molybdenum−tin composite oxide catalyst (H−Mo1Sn2, a molar ratio of Mo/Sn = 1:2) was synthesized *via* the hydrothermal method using $(NH_4)_6MoO_7O_{24}\cdot 4H_2O$ and $SnCl_4\cdot 5H_2O$ as the precursors of Mo and Sn. Simply, well-weighted $SnCl_4\cdot 5H_2O$ was added into the solution containing $(NH_4)_6MoO_7O_{24}\cdot 4H_2O$ at 60 °C. After rigorous stirring for 1 h, the suspension was transferred into a PTFE-lined stainless-steel autoclave and hydrothermally treated for 24 h. After that, the solid product was collected *via* centrifugation and drying. Further calcination to the above product at different atmospheres and 500 °C (for 8 h) is used to obtain the needed catalysts such as H−Mo1Sn2-Air (also referred to as H−Mo1Sn2) and H−Mo1Sn2-O_2. The comparison catalysts were also prepared by referring to literature methods,[17,18] including the coprecipitation method (C−Mo1Sn2), impregnation method (I−Mo1Sn2), and mechanic mixing method (M-Mo1Sn2). Detailed processes can be found in the Supporting Information.

Catalyst Characterization

The high-resolution transmission electron microscopy (HRTEM) images were obtained on a JEOL JEM 2100 TEM, operating at 200 kV. Aberration-corrected high-angle annular dark-field scanning transmission electron microscopy (AC HAADF-STEM) was performed by using an aberration-corrected Titan Cubed Themis G2300 instrument. X-ray photoelectron spectra (XPS) and *quasi in situ* XPS were recorded on an AXIS ULTRA DLD X-ray photoelectron spectrometer (Kratos Co.) equipped with an Al Kα X-ray excitation source ($h\nu$ = 1486.6 eV). Low-temperature electron spin resonance (ESR) spectra were recorded on a Bruker EMX plus-10/12 spectrometer, operating in the X-band (at 9.41 GHz) with a 100 kHz magnetic field modulation at −173 °C. X-ray absorption fine structure (XAFS) and *in situ* XAFS data at the Mo K-edge (20.0 keV) and Sn K-edge (29.2 keV) of the samples were recorded on the BL14W1 beamline of the Shanghai Synchrotron Radiation Facility (SSRF), with operation in transmission mode using an ion chamber and a Si(311) crystal monochromator. The X-ray absorption near-edge spectroscopy (XANES) and extended X-ray absorption fine structure (EXAFS) data were analyzed with the Athena and Artemis programs. For the wavelet transform analysis (WTA), the (k) exported from Athena was introduced to the Hama Fortran code, using the parameters of R range (1−6 Å), k range (0−12 Å^{-1}), and k weight (2). Morlet function with κ = 10, σ = 1 was applied as the mother wavelet to provide the overall distribution.[52] Dimethyl ether temperature-programmed surface reaction and mass spectrometry (DME-TPSR-MS) experiments were performed in a fixed-bed reactor system combined with an online mass spectrometer. An $^{18}O_2$ isotope tracer IR and mass spectrometry ($^{18}O_2$−IR-MS) experiments were performed on a Bruker Tensor 27 with an MCT detector (64 scans, 4 cm^{-1}) combined with an online mass spectrometer detector. Full details of the characterizations are revealed in the Supporting Information.

Catalytic Activity Measurement

All of the catalysts were crushed to 20−40 mesh prior to catalytic evaluation. The reaction was carried out in a fixed-bed reactor at atmospheric pressure (using 1 mL of catalyst). For each test, the catalyst was first activated at 300 °C for 2 h under an O_2 atmosphere. After cooling to the reaction temperatures (110 or 150 °C), DME was introduced into the reactor. The molar ratio of DME:O_2 was 1:1 and the total gas hourly space velocity (GHSV) was 1800 h^{-1}.

Product Analysis and Quantification

Quantitative analysis of products was carried out on three gas chromatographs (GC). Organic oxygenates ($HCOOCH_3$, CH_3OH, HCHO, and $CH_3OCH_2OCH_3$) were analyzed by a GC-2014CPF/SPL (Shimadzu) gas chromatograph equipped with a flame ionization detector (FID, DB-1 capillary column) and a GC-2014 (Shimadzu) equipped with a thermal conductivity detector (TCD, Porapak T column). H_2, CO, CO_2, and CH_4 were analyzed by a GC-4000 instrument (Beijing EWAI). The methods for the calculation of conversion and selectivity are displayed in the Supporting Information.

Theoretical Calculation

Density functional theory (DFT) with the PBE (Perdew−Burke−Ernzerhof) functional is implemented in the CP2K package[53−55] and the Vienna Ab initio Simulation Package (VASP).[56−58] The interactions between the MoO_x cluster and SnO_2 were investigated by density functional theory (DFT). Before calculation, the parameters adopted in the procedure of optimization were tested. Ab initio molecular dynamics (AIMD) simulations starting from the optimized structure were used to study the effects of O_2 on the structural evolution of Mo_9O_x/SnO_2 (110) catalysts. The adsorption and activation of DME were investigated on a MoO_x cluster loaded on the surface of SnO_2 (110). To study the catalysis of Mo and Sn, the reactions including DME dissociation, HCHO formation through CH_3O*, and the formation of H_2COOCH_3* and MF all fall in our consideration. During calculation, the DFT + U method was adopted to make a better description of the strongly interacted metal oxide systems, where U = 5.0 and 4.0 eV were used for Mo and Sn 4d electrons, respectively. More details of the theoretical calculation are provided in the Supporting Information.

ASSOCIATED CONTENT

Supporting Information

The Supporting Information is available free of charge at https://pubs.acs.org/doi/10.1021/jacsau.3c00479.

Experimental procedures; characterization results, evaluation data, and theoretical calculation data (PDF)

AUTHOR INFORMATION

Corresponding Authors

Tao Zhang − *State Key Laboratory of Coal Conversion, Institute of Coal Chemistry, Chinese Academy of Sciences, Taiyuan 030001 Shanxi, China*; Email: zhangtao@sxicc.ac.cn

Junfeng Zhang − *State Key Laboratory of Coal Conversion, Institute of Coal Chemistry, Chinese Academy of Sciences, Taiyuan 030001 Shanxi, China*; orcid.org/0000-0002-7909-3179; Email: zhangjf@sxicc.ac.cn

Qingde Zhang − *State Key Laboratory of Coal Conversion, Institute of Coal Chemistry, Chinese Academy of Sciences, Taiyuan 030001 Shanxi, China; Dalian National Laboratory for Clean Energy, Dalian 116023, China;*

https://doi.org/10.1021/jacsau.3c00479
JACS Au 2023, 3, 3141−3154

orcid.org/0000-0002-8022-1916; Email: qdzhang@sxicc.ac.cn

Authors

Qi Yang − *State Key Laboratory of Coal Conversion, Institute of Coal Chemistry, Chinese Academy of Sciences, Taiyuan 030001 Shanxi, China; University of Chinese Academy of Sciences, Beijing 100049, China*

Xiujuan Gao − *State Key Laboratory of Coal Conversion, Institute of Coal Chemistry, Chinese Academy of Sciences, Taiyuan 030001 Shanxi, China; University of Chinese Academy of Sciences, Beijing 100049, China*

Faen Song − *State Key Laboratory of Coal Conversion, Institute of Coal Chemistry, Chinese Academy of Sciences, Taiyuan 030001 Shanxi, China*

Xiaoxing Wang − *State Key Laboratory of Coal Conversion, Institute of Coal Chemistry, Chinese Academy of Sciences, Taiyuan 030001 Shanxi, China;* orcid.org/0000-0002-2094-1081

Pan Xiong − *State Key Laboratory of Coal Conversion, Institute of Coal Chemistry, Chinese Academy of Sciences, Taiyuan 030001 Shanxi, China; University of Chinese Academy of Sciences, Beijing 100049, China*

Yunxing Bai − *State Key Laboratory of Coal Conversion, Institute of Coal Chemistry, Chinese Academy of Sciences, Taiyuan 030001 Shanxi, China; University of Chinese Academy of Sciences, Beijing 100049, China*

Xingchen Liu − *State Key Laboratory of Coal Conversion, Institute of Coal Chemistry, Chinese Academy of Sciences, Taiyuan 030001 Shanxi, China;* orcid.org/0000-0002-9704-5728

Xiaoyan Liu − *Dalian Institute of Chemical Physics, Chinese Academy of Science, Dalian 116023, China;* orcid.org/0000-0003-2694-2306

Gang Fu − *State Key Laboratory of Physical Chemistry of Solid Surfaces, Xiamen University, Xiamen 361005, China;* orcid.org/0000-0003-3141-2190

Yisheng Tan − *State Key Laboratory of Coal Conversion, Institute of Coal Chemistry, Chinese Academy of Sciences, Taiyuan 030001 Shanxi, China;* orcid.org/0000-0003-3148-3730

Yizhuo Han − *State Key Laboratory of Coal Conversion, Institute of Coal Chemistry, Chinese Academy of Sciences, Taiyuan 030001 Shanxi, China*

Complete contact information is available at: https://pubs.acs.org/10.1021/jacsau.3c00479

Author Contributions

CRediT: **Qi Yang** data curation, investigation, methodology, software, visualization, writing-original draft, writing-review & editing; **Xiujuan Gao** formal analysis, methodology, writing-review & editing; **Faen Song** methodology, writing-review & editing; **Xiaoxing Wang** methodology, writing-review & editing; **Tao Zhang** methodology, software, writing-original draft, writing-review & editing; **Pan Xiong** data curation, investigation; **Yunxing Bai** methodology, writing-review & editing; **Xingchen Liu** writing-review & editing; **Xiaoyan Liu** methodology, writing-review & editing; **Junfeng Zhang** methodology, writing-review & editing; **Gang Fu** methodology, writing-review & editing; **Yisheng Tan** resources, writing-review & editing; **Yizhuo Han** methodology, writing-review & editing; **Qingde Zhang** conceptualization, funding acquisition, investigation, project administration, resources, supervision, validation, writing-review & editing.

Notes

The authors declare no competing financial interest.

■ ACKNOWLEDGMENTS

This work was financially supported by the National Natural Science Foundation of China (Nos. 22172187 and 21773283), the Central Guidance on Local Science and Technology Development Fund of Shanxi Province (No. YDZJSX2022A073), the Dalian National Laboratory for Clean Energy (DNL) Cooperation Fund, CAS (DNL 201903), the CAS Interdisciplinary Innovation Team (BK2018001), the Youth Innovation Promotion Association CAS (No. 2014155), and the Open Project Program of the State Key Laboratory of Physical Chemistry of Solid Surfaces, Xiamen University (No.201624). The authors are grateful to the BL14W1 station in Shanghai Synchrotron Radiation Facility (SSRF) for the XAFS measurement.

■ ABBREVIATIONS

DME	dimethyl ether
ESR	electron spin resonance
MF	methyl formate
XPS	X-ray photoelectron spectra
XAFS	X-ray absorption fine structure
SSRF	Shanghai Synchrotron Radiation Facility
XANES	X-ray absorption near-edge spectroscopy
EXAFS	extended X-ray absorption fine structure
FT-EXAFS	Fourier-transformed extended X-ray absorption fine structure
WTA	wavelet transform analysis
CN	coordination number
TEM	transmission electron microscopy
HRTEM	high-resolution transmission electron microscopy
AC HAADA-STEM	aberration-corrected high-angle annular dark-field scanning transmission electron microscopy
TPSR	temperature-programmed surface reaction
DME-TPSR-MS	dimethyl ether temperature-programmed surface reaction and mass spectrometry
$^{18}O_2$−IR-MS	$^{18}O_2$ isotope tracer IR experiment and mass spectrometry
GHSV	gas hourly space velocity
GC	gas chromatographs
FID	flame ionization detector
TCD	thermal conductivity detector
DFT	density functional theory
PBE	Perdew−Burke−Ernzerhof
VASP	Vienna Ab initio Simulation Package
XRD	X-ray powder diffraction
EDX	energy-dispersive X-ray spectroscopy
HREELS	high-resolution electron energy loss spectroscopy
AIMD	ab initio molecular dynamics
H−Mo1Sn2	molybdenum−tin composite oxide catalyst prepared by a hydrothermal method
C−Mo1Sn2	molybdenum−tin composite oxide catalyst prepared by the coprecipitation method

https://doi.org/10.1021/jacsau.3c00479
JACS Au 2023, 3, 3141−3154

I−Mo1Sn2	molybdenum−tin composite oxide catalyst prepared by the impregnation method
M-Mo1Sn2	molybdenum−tin composite oxide catalyst prepared by the mechanic mixing method

REFERENCES

(1) Guo, Z.; Liu, B.; Zhang, Q.; Deng, W.; Wang, Y.; Yang, Y. Recent advances in heterogeneous selective oxidation catalysis for sustainable chemistry. *Chem. Soc. Rev.* **2014**, *43*, 3480−3524.

(2) Gao, X.; Zhang, J.; Song, F.; Zhang, Q.; Han, Y.; Tan, Y. Selective oxidation conversion of methanol/dimethyl ether. *Chem. Commun.* **2022**, *58*, 4687−4699.

(3) Xie, J.; Jin, R.; Li, A.; Bi, Y.; Ruan, Q.; Deng, Y.; Zhang, Y.; Yao, S.; Sankar, G.; Ma, D.; Tang, J. Highly selective oxidation of methane to methanol at ambient conditions by titanium dioxide-supported iron species. *Nat. Catal.* **2018**, *1*, 889−896.

(4) Kaichev, V. V.; Popova, G. Y.; Chesalov, Y. A.; Saraev, A. A.; Zemlyanov, D. Y.; Beloshapkin, S. A.; Knop-Gericke, A.; Schlogl, R.; Andrushkevich, T. V.; Bukhtiyarov, V. I. Selective oxidation of methanol to form dimethoxymethane and methyl formate over a monolayer V_2O_5/TiO_2 catalyst. *J. Catal.* **2014**, *311*, 59−70.

(5) Wang, Y. Room-temperature conversion of methane becomes true. *Joule* **2018**, *2*, 1399−1401.

(6) Cui, X. J.; Li, H. B.; Wang, Y.; Hu, Y. L.; Hua, L.; Li, H. Y.; Han, X. W.; Liu, Q. F.; Yang, F.; He, L. M.; Chen, X. Q.; Li, Q. Y.; Xiao, J. P.; Deng, D. H.; Bao, X. H. Room-temperature methane conversion by graphene-confined single iron atoms. *Chem* **2018**, *4*, 1902−1910.

(7) Anastas, P. T.; Kirchhoff, M. M. Origins, current status, and future challenges of green chemistry. *Acc. Chem. Res.* **2002**, *35*, 686−694.

(8) de Castro, I. A.; Datta, R. S.; Ou, J. Z.; Castellanos-Gomez, A.; Sriram, S.; Daeneke, T.; Kalantar-Zadeh, K. Molybdenum oxides - From fundamentals to functionality. *Adv. Mater.* **2017**, *29*, No. 1701619.

(9) Liu, H. C.; Cheung, P.; Iglesia, E. Structure and support effects on the selective oxidation of dimethyl ether to formaldehyde catalyzed by MoO_x domains. *J. Catal.* **2003**, *217*, 222−232.

(10) Handzlik, J.; Sautet, P. Structure of dimeric molybdenum(VI) oxide species on γ-alumina: A periodic density functional theory study. *J. Phys. Chem. C* **2010**, *114*, 19406−19414.

(11) Wang, F.; Ueda, W. High catalytic efficiency of nanostructured molybdenum trioxide in the benzylation of arenes and an investigation of the reaction mechanism. *Chem. - Eur. J.* **2009**, *15*, 742−753, DOI: 10.1002/chem.200801153.

(12) Thielemann, J. P.; Hess, C. Monitoring silica supported molybdenum oxide catalysts at work: A Raman spectroscopic study. *ChemPhysChem* **2013**, *14*, 441−447.

(13) Šustek, M.; Horváth, B.; Vávra, I.; Gál, M.; Dobročka, E.; Hronec, M. Effects of structures of molybdenum catalysts on selectivity in gas-phase propylene oxidation. *Chin. J. Catal.* **2015**, *36*, 1900−1909.

(14) Liu, G. B.; Zhang, Q. D.; Han, Y. Z.; Tsubaki, N.; Tan, Y. S. Selective oxidation of dimethyl ether to methyl formate over trifunctional MoO_3-SnO_2 catalyst under mild conditions. *Green Chem.* **2013**, *15*, 1501−1504.

(15) Zhang, Q. D.; Tan, Y. S.; Liu, G. B.; Zhang, J. F.; Han, Y. Z. Rhenium oxide-modified $H_3PW_{12}O_{40}/TiO_2$ catalysts for selective oxidation of dimethyl ether to dimethoxy dimethyl ether. *Green Chem.* **2014**, *16*, 4708−4715.

(16) Sun, J.; Yang, G. H.; Yoneyama, Y.; Tsubaki, N. Catalysis chemistry of dimethyl ether synthesis. *ACS Catal.* **2014**, *4*, 3346−3356.

(17) Liu, G. B.; Zhang, Q. D.; Han, Y. Z.; Tsubaki, N.; Tan, Y. S. Effects of the MoO_3 structure of Mo-Sn catalysts on dimethyl ether oxidation to methyl formate under mild conditions. *Green Chem.* **2015**, *17*, 1057−1064.

(18) Zhang, Z.; Zhang, Q.; Jia, L.; Wang, W.; Tian, S. P.; Wang, P.; Xiao, H.; Han, Y.; Tsubaki, N.; Tan, Y. The effects of the Mo-Sn contact interface on the oxidation reaction of dimethyl ether to methyl formate at a low reaction temperature. *Catal. Sci. Technol.* **2016**, *6*, 6109−6117.

(19) Dieterle, M.; Weinberg, G.; Mestl, G. Raman spectroscopy of molybdenum oxides - Part I. Structural characterization of oxygen defects in MoO_{3-x} by DR UV/VIS, Raman spectroscopy and X-ray diffraction. *Phys. Chem. Chem. Phys.* **2002**, *4*, 812−821.

(20) Dieterle, M.; Mestl, G. Raman spectroscopy of molybdenum oxides - Part II. Resonance Raman spectroscopic characterization of the molybdenum oxides Mo_4O_{11} and MoO_2. *Phys. Chem. Chem. Phys.* **2002**, *4*, 822−826.

(21) Zhang, Z. Z.; Zhang, Q. D.; Jia, L. Y.; Wang, W. F.; Gao, X. F.; Gu, Y. Y.; Gao, X. J.; Han, Y. Z.; Tan, Y. S. Regulation of SBA-15, gamma-Al_2O_3, ZSM-5 and MgO on molybdenum oxide and consequent effect on DME oxidation reaction. *ChemistrySelect* **2016**, *1*, 6127−6135.

(22) Liu, M. M.; Tang, W. Q.; Xie, Z. H.; Yu, H. B.; Yin, H. F.; Xu, Y. S.; Zhao, S. L.; Zhou, S. H. Design of highly efficient Pt-SnO_2 hydrogenation nanocatalysts using Pt@Sn core-shell nanoparticles. *ACS Catal.* **2017**, *7*, 1583−1591.

(23) Murugappan, K.; Anderson, E. M.; Teschner, D.; Jones, T. E.; Skorupska, K.; Roman-Leshkov, Y. Operando NAP-XPS unveils differences in MoO_3 and Mo_2C during hydrodeoxygenation. *Nat. Catal.* **2018**, *1*, 960−967.

(24) Vasilopoulou, M.; Douvas, A. M.; Georgiadou, D. G.; Palilis, L. C.; Kennou, S.; Sygellou, L.; Soultati, A.; Kostis, I.; Papadimitropoulos, G.; Davazoglou, D.; Argitis, P. The influence of hydrogenation and oxygen vacancies on molybdenum oxides work function and gap states for application in organic optoelectronics. *J. Am. Chem. Soc.* **2012**, *134*, 16178−16187.

(25) Zhang, Z. S.; Fu, Q.; Xu, K.; Wang, W. W.; Fu, X. P.; Zheng, X. S.; Wu, K.; Ma, C.; Si, R.; Jia, C. J.; Sun, L. D.; Yan, C. H. Intrinsically active surface in a Pt/gamma-Mo_2N catalyst for the water-gas shift reaction: Molybdenum nitride or molybdenum oxide? *J. Am. Chem. Soc.* **2020**, *142*, 13362−13371.

(26) Wu, J.; Fan, J.; Zhao, X.; Wang, Y.; Wang, D.; Liu, H.; Gu, L.; Zhang, Q.; Zheng, L.; Singh, D. J.; Cui, X.; Zheng, W. Atomically dispersed MoO_x on rhodium metallene boosts electrocatalyzed alkaline hydrogen evolution. *Angew. Chem., Int. Ed.* **2022**, *61*, No. e202207512, DOI: 10.1002/anie.202207512.

(27) Lajaunie, L.; Boucher, F.; Dessapt, R.; Moreau, P. Quantitative use of electron energy-loss spectroscopy Mo-$M_{2,3}$ edges for the study of molybdenum oxides. *Ultramicroscopy* **2015**, *149*, 1−8.

(28) Young, C. G. Chemical systems modeling the d(1) Mo(V) states of molybdenum enzymes. *J. Inorg. Biochem.* **2016**, *162*, 238−252.

(29) Lakshmi, L. J.; Alyea, E. C. ESR, FT-Raman spectroscopic and ethanol partial oxidation studies on MoO_3/SnO_2 catalysts made by metal oxide vapor synthesis. *Catal. Lett.* **1999**, *59*, 73−77.

(30) Ruslan, N. N.; Triwahyono, S.; Jalil, A. A.; Timmiati, S. N.; Annuar, N. H. R. Study of the interaction between hydrogen and the MoO_3-ZrO_2 catalyst. *Appl. Catal., A* **2012**, *413-414*, 176−182.

(31) Che, M.; Sojka, Z. Electron transfer processes at the surface of MoO_x/SiO_2 catalysts. *Top. Catal.* **2001**, *15*, 211−217.

(32) Kim, H. S.; Cook, J. B.; Lin, H.; Ko, J. S.; Tolbert, S. H.; Ozolins, V.; Dunn, B. Oxygen vacancies enhance pseudocapacitive charge storage properties of MoO_{3-x}. *Nat. Mater.* **2017**, *16*, 454−460.

(33) Tong, Y.; Chen, P. Z.; Zhang, M. X.; Zhou, T. P.; Zhang, L. D.; Chu, W. S.; Wu, C. Z.; Xie, Y. Oxygen vacancies confined in nickel molybdenum oxide porous nanosheets for promoted electrocatalytic urea oxidation. *ACS Catal.* **2018**, *8*, 1−7.

(34) Yu, H. S.; Wei, X. J.; Li, J.; Gu, S. Q.; Zhang, S.; Wang, L. H.; Ma, J. Y.; Li, L. N.; Gao, Q.; Si, R.; Sun, F. F.; Wang, Y.; Song, F.; Xu, H. J.; Yu, X. H.; Zou, Y.; Wang, J. Q.; Jiang, Z.; Huang, Y. Y. The XAFS beamline of SSRF. *Nucl. Sci. Technol.* **2015**, *26*, No. 050102, DOI: 10.13538/j.1001-8042/nst.26.050102.

https://doi.org/10.1021/jacsau.3c00479
JACS Au 2023, 3, 3141−3154

(35) Brookes, C.; Bowker, M.; Gibson, E. K.; Gianolio, D.; Mohammed, K. M. H.; Parry, S.; Rogers, S. M.; Silverwood, I. P.; Wells, P. P. *In situ* spectroscopic investigations of MoO_x/Fe_2O_3 catalysts for the selective oxidation of methanol. *Catal. Sci. Technol.* **2016**, *6*, 722−730.
(36) Okamoto, Y.; Oshima, N.; Kobayashi, Y.; Terasaki, O.; Kodaira, T.; Kubota, T. Structure of intrazeolite molybdenum oxide clusters and their catalysis of the oxidation of ethyl alcohol. *Phys. Chem. Chem. Phys.* **2002**, *4*, 2852−2862.
(37) Nair, H.; Gatt, J. E.; Miller, J. T.; Baertsch, C. D. Mechanistic insights into the formation of acetaldehyde and diethyl ether from ethanol over supported VO_x, MoO_x, and WO_x catalysts. *J. Catal.* **2011**, *279*, 144−154.
(38) Stashans, A.; Puchaicela, P.; Rivera, R. DFT study of chromium-doped SnO_2 materials. *J. Mater. Sci.* **2014**, *49*, 2904−2911.
(39) Inzani, K.; Grande, T.; Vullum-Bruer, F.; Selbach, S. M. A van der Waals density functional study of MoO_3 and its oxygen vacancies. *J. Phys. Chem. C* **2016**, *120*, 8959−8968.
(40) Cheung, P.; Liu, H. C.; Iglesia, E. Kinetics and mechanism of dimethyl ether oxidation to formaldehyde on supported molybdenum oxide domains. *J. Phys. Chem. B* **2004**, *108*, 18650−18658.
(41) Wojcieszak, R.; Karelovic, A.; Gaigneaux, E. M.; Ruiz, P. Oxidation of methanol to methyl formate over supported Pd nanoparticles: insights into the reaction mechanism at low temperature. *Catal. Sci. Technol.* **2014**, *4*, 3298−3305.
(42) Chung, M.; Moon, D.; Park, K.; Ihm, S. Mechanism of methyl formate formation on Cu/ZnO catalysts. *J. Catal.* **1992**, *136*, 609−612.
(43) Cheng, W.-H. Methanol and Formaldehyde Oxidation Study over Molybdenum Oxide. *J. Catal.* **1996**, *158*, 477−485.
(44) Huang, X. M.; Liu, J. L.; Chen, J. L.; Xu, Y. D.; Shen, W. J. Mechanistic study of selective oxidation of dimethyl ether to formaldehyde over alumina-supported molybdenum oxide catalyst. *Catal. Lett.* **2006**, *108*, 79−86.
(45) Góra-Marek, K. IR studies of the transformation of formaldehyde and methanol on Co-ferrierites. *Microporous Mesoporous Mater.* **2011**, *145*, 93−97.
(46) Matyshak, V. A.; Sil'chenkova, O. N.; Ismailov, I. T.; Tret'yakov, V. F. Mechanism of methanol conversion on ZrO_2 and $5\%Cu/ZrO_2$ according to in situ IR spectroscopic data. *Kinet. Catal.* **2010**, *51*, 428−437.
(47) Finocchio, E.; Daturi, M.; Binet, C.; Lavalley, J. C.; Blanchard, G. Thermal evolution of the adsorbed methoxy species on $Ce_xZr_{1-x}O_2$ solid solution samples: a FT-IR study. *Catal. Today* **1999**, *52*, 53−63.
(48) Reece, C.; Redekop, E. A.; Karakalos, S.; Friend, C. M.; Madix, R. J. Crossing the great divide between single-crystal reactivity and actual catalyst selectivity with pressure transients. *Nat. Catal.* **2018**, *1*, 852−859.
(49) Yang, H.; Chen, Y.; Cui, X.; Wang, G.; Cen, Y.; Deng, T.; Yan, W.; Gao, J.; Zhu, S.; Olsbye, U.; Wang, J.; Fan, W. A highly stable copper-based catalyst for clarifying the catalytic roles of Cu^0 and Cu^+ species in methanol dehydrogenation. *Angew. Chem., Int. Ed.* **2018**, *57*, 1836−1840.
(50) Gercher, V. A.; Cox, D. F.; Themlin, J.-M. Oxygen-vacancy-controlled chemistry on a metal oxide surface: methanol dissociation and oxidation on $SnO_2(110)$. *Surf. Sci.* **1994**, *306*, 279−293.
(51) Cant, N. W.; Tonner, S. P.; Trimm, D. L.; Wainwright, M. S. Isotopic labeling studies of the mechanism of dehydrogenation of methanol to methyl formate over copper-based catalysts. *J. Catal.* **1985**, *91*, 197−207.
(52) Xia, Z.; Zhang, H.; Shen, K.; Qu, Y.; Jiang, Z. Wavelet analysis of extended X-ray absorption fine structure data: Theory, application. *Phys. B* **2018**, *542*, 12−19.
(53) Kühne, T. D.; Iannuzzi, M.; Del Ben, M.; Rybkin, V. V.; Seewald, P.; Stein, F.; Laino, T.; Khaliullin, R. Z.; Schütt, O.; Schiffmann, F.; Golze, D.; Wilhelm, J.; Chulkov, S.; Bani-Hashemian, M. H.; Weber, V.; Borštnik, U.; Taillefumier, M.; Jakobovits, A. S.; Lazzaro, A.; Pabst, H.; Müller, T.; Schade, R.; Guidon, M.; Andermatt, S.; Holmberg, N.; Schenter, G. K.; Hehn, A.; Bussy, A.; Belleflamme, F.; Tabacchi, G.; Glöß, A.; Lass, M.; Bethune, I.; Mundy, C. J.; Plessl, C.; Watkins, M.; VandeVondele, J.; Krack, M.; Hutter, J. CP2K: An electronic structure and molecular dynamics software package - Quickstep: Efficient and accurate electronic structure calculations. *J. Chem. Phys.* **2020**, *152*, No. 194103, DOI: 10.1063/5.0007045.
(54) VandeVondele, J.; Hutter, J. Gaussian basis sets for accurate calculations on molecular systems in gas and condensed phases. *J. Chem. Phys.* **2007**, *127*, No. 114105.
(55) Perdew, J. P.; Burke, K.; Ernzerhof, M. Generalized gradient approximation made simple. *Phys. Rev. Lett.* **1996**, *77*, 3865−3868.
(56) Kresse, G.; Hafner, J. Ab initio molecular-dynamics simulation of the liquid-metal-amorphous-semiconductor transition in germanium. *Phys. Rev. B* **1994**, *49*, 14251−14269.
(57) Kresse, G.; Furthmüller, J. Efficient iterative schemes for ab initio total-energy calculations using a plane-wave basis set. *Phys. Rev. B* **1996**, *54*, 11169−11186.
(58) Kresse, G.; Furthmüller, J. Efficiency of ab-initio total energy calculations for metals and semiconductors using a plane-wave basis set. *Comput. Mater. Sci.* **1996**, *6*, 15−50.

https://doi.org/10.1021/jacsau.3c00479
JACS Au 2023, 3, 3141−3154